

Characterization of UFG materials by X-ray and Neutron diffraction

T Ungár^{1,2}, G Ribárik¹

² Department of Materials Physics, Eötvös University, H-1117 Budapest, Hungary

³ Materials Performance Centre, School of Materials, The University of Manchester, Manchester M13 9PL, UK

Corresponding author: ungar@ludens.elte.hu

Abstract. Grain size, subgrain size, microstrain, dislocation density and dislocation types and intergranular strains determine the mechanical, chemical and other physical properties in materials of submicron grain size. Electron microscopy is a straightforward method to determine the substructure. X-ray and neutron diffraction methods supplement dynamic properties, especially strains and stresses and number densities of substructure elements. The synergy of electron microscopy and diffraction patterns provides a more comprehensive characterization of the substructure and a better understanding of the performance of ultra-fine-grain (UFG) materials.

1. Introduction

X-ray and neutron diffraction line-profile-analysis (LPA) proved to be a powerful tool for determining the sub-structure of crystalline materials in terms of (i) grain size or subgrain size, (ii) dislocation density and dislocation type, (iii) twinning and faulting and (iv) other types of lattice defects. The convolutional multiple whole profile (CMWP) method of LPA procedure is based on physically modeled profile functions of the different microstructural elements, and is available as a free software package. In the present work, a few of applications to determine the dislocation structure in severe plastic deformed bulk nanocrystalline materials will follow a brief summary of the diffraction procedure. At the end, the paper provides a comprehensive list of relevant references.

2. Basic principles of line profile analysis

Within the frame of the kinematical scattering theory, the intensity distribution diffracted from a large defect-free crystal is similar to a δ function, i.e. its breadth is zero, and however its maximum is finite. When (i) the scattering crystal becomes smaller than about a micron [1-4], or when it contains (ii) dislocations [5-8], (iii) planar defects [9-12], (iv) chemical inhomogeneities [13], (v) lattice strains [14] or other types of lattice defects [15], the diffraction peaks broaden. There are two fundamentally different broadening types: (1) size-broadening and (2) strain broadening. Size broadening is diffraction order independent. The broadening of diffraction peaks stays globally constant in reciprocal space. Strain broadening, however, increases, also in a global manner as a function of distance from the origin of the reciprocal space. Both types of broadening can vary for different hkl -s. In the case of size broadening the hkl variation is caused by shape anisotropy [16,17], whereas in the case of strain broadening the hkl dependence is produced by strain anisotropy [7,18]. Strain anisotropy in line broadening means that neither the breadths in a Williamson-Hall plot [19] nor the Fourier



coefficients in the Warren-Averbach method [2] increase or decrease monotonously as a function of g or g^2 , respectively, where g is the absolute value of the diffraction vector. A large variety of lattice defects cause strain in a crystal. There is a strong correlation between the space dependence of strain fields and the dimensionality of the different lattice defects [5]. Point defects, GP-zones, small precipitates, small dislocation loops or small second phase particles have zero dimension and the strain field is of short range character, i.e. $\varepsilon(r) \cong 1/r^2$. Dislocations are one dimensional defects and the strain fields are of long range character, i.e. $\varepsilon(r) \cong 1/r$. Different types of planar defects are two dimensional defects and the strain fields are homogeneous, i.e. $\varepsilon(r) \cong \text{constant}$. Since there is reciprocity in the distance relation between crystal and reciprocal space, short-range strain fields will cause diffraction far from the Bragg peaks, whereas long-range strain fields will cause diffraction clustered around the Bragg peaks. The former is slowly varying diffuse scattering below the Bragg peaks, whereas latter is line broadening. Homogeneous strain fields, corresponding to two dimensional lattice defects, like planar defects, cause peak shifts [2,9-12]. This relatively simple dimensional consideration is the dislocation theorem of line broadening [5,6,18]. It means that strain broadening always indicates the presence of linear type lattice defects, i.e. the presence of dislocations.

The Fourier transform of the strain profile is [2]:

$$A_{hkl}^D(L) \cong \exp[-2\pi^2 g^2 L^2 \langle \varepsilon_{g,L}^2 \rangle], \quad (1)$$

where L is the Fourier variable and $\langle \varepsilon_{g,L}^2 \rangle$ is the mean square strain. Krivoglaz [5] and Wilkens [6] derived the mean square strain for dislocated crystals:

$$\langle \varepsilon_{g,L}^2 \rangle = \frac{\rho C b^2}{4\pi} f(\eta), \quad (2)$$

where ρ , C and b are the density, the contrast factor and the Burgers vector absolute values of dislocations. The function $f(\eta)$ describes the L dependence of the mean-square-strain, $\eta = L/R_e$, where R_e is the effective outer cut-off radius of dislocations. R_e in eq. (2) is the same physical quantity as the effective outer cut-off radius of dislocations in the elastic stored energy of dislocated crystals [20]. R_e only makes sense in relation to the average distance of dislocations: $d = 1/\sqrt{\rho}$ [6]. If R_e is small or large relative to d , the dislocations are in a stronger or weaker dipole configuration. The dislocation arrangement parameter $M = R_e \sqrt{\rho}$ gives the dipole character, or the effectiveness of strain field screening [6]. If M is smaller or larger than unity the dipole character, or the screening of strain fields, of dislocations is stronger or weaker, respectively. The M parameter is in direct correlation with the profile shape in the lowest intensity range. For stronger or weaker dipole character, the tails of the diffraction peaks will be longer or shorter, respectively. The full-width-at-half-maximum (FWHM) of diffraction peaks is only one part of line broadening. The other, more decisive part is the tail region [5,6]. Fig. 1a shows the 200 diffraction profiles measured at the surface (solid line) and in the bulk (dashed line) of a Cu single crystal oriented for single slip and tensile deformed to a shear strain of $\gamma = 0.43$ at RT [21]. The two profiles were measured on the crystal surface where the unpaired edge components of the dislocation dipoles escaped from the near surface region. In this or in the bulk region the dislocation arrangement has a weaker or stronger dipole character, respectively. The dislocation density in the bulk is larger than what the increase of FWHM would predict alone. Figure 1b shows the changing of dislocation density and arrangement parameter vs. the distance from the surface in the primary slip direction. Fig. 1c shows the same profile shape behavior in a high-pressure torsion (HPT) deformed Cu-10%Zn alloy [22]. The 8 mm diameter diskette was HPT deformed by 6 GPa pressure and 5 rotations. The figure shows the 220 reflections for the center (blue line) and the edge (red line) regions of the specimen, where the M parameter values are 2.6 and 1.3, respectively. The ratio of the FWHM values of the 220 reflections is $R_{\text{FWHM}} = 1.57$, whereas the ratio of the

dislocation densities is $R_p=5.9$. The value of R_p is by far larger than R_{FWHM} , in correlation that, at larger dislocation densities the dipole character is usually stronger.

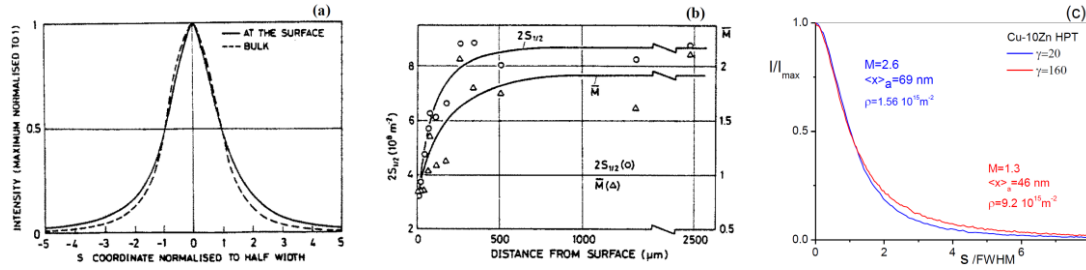


Figure 1. (a) The 200 peak profiles measured on the surface and in the bulk, (b) the FWHM ($2S_{1/2}$) and the M parameter vs. the distance from the surface in a tensile deformed Cu single crystal [21]. (c) The profile shape of 220 reflections for the center (blue line) and the edge (red line) regions of a HPT deformed Cu-10%Zn alloy [22]. (By courtesy of [21,22]).

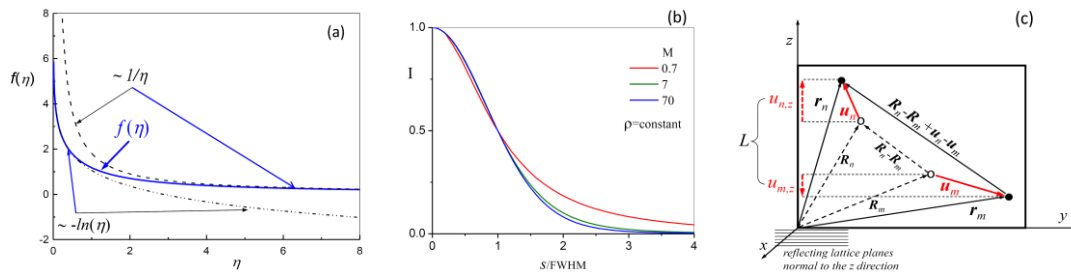


Figure 2. (a) The dash double-dot and the dashed line are logarithmic and the hyperbolic asymptotes at small and large η values, respectively. The blue solid line is the numerical matching of the two asymptotic functions having smooth derivatives.

Krivoglaz derived eq. (2) for small L values where $\langle \epsilon_{g,L}^2 \rangle$ has a logarithmic singularity [5]. Wilkens derived $\langle \epsilon_{g,L}^2 \rangle$ in the entire L range and showed that at large L values it is hyperbolic. Fig. 2a shows the $f(\eta)$ function [6]. Consistently with experiment, the average density, ρ and the arrangement parameter, M describe the dislocation structure. The replacement of the $\langle \epsilon_{g,L}^2 \rangle$ function by a single number, e.g. in the Williamson-Hall method, automatically assumes that the strain profile is a pure Gaussian function. The experimental Figs. 1a and 1c show that this is almost never the case. A single number cannot replace the $\langle \epsilon_{g,L}^2 \rangle$ function.

The term "mean square strain" is rather misleading. The scattered intensity, $I(K)$, is the square of the scattered amplitudes of waves. Fig. 2c shows schematically the relation between $\langle \epsilon_{g,L}^2 \rangle$ and lattice distortions, \mathbf{u} . Line broadening is determined by the pair-correlation of atomic displacements, \mathbf{u}_n and \mathbf{u}_m at distances between the two positions, $\mathbf{r}_n - \mathbf{r}_m$. Quantitatively the pair-correlation of atomic displacements is given by the non-local distortion tensor, β [5,6,23]:

$\mathbf{r}_n - \mathbf{r}_m = \mathbf{R}_n - \mathbf{R}_m + \mathbf{u}_n - \mathbf{u}_m = [1 + \underline{\beta}(\mathbf{R}_n, \mathbf{R}_m)](\mathbf{R}_n - \mathbf{R}_m)$, and the correspondence between β , and the infinitesimal strain tensor, $\underline{\hat{\beta}} = \text{grad} \mathbf{u}$ is: $\mathbf{u}_n - \mathbf{u}_m = \underline{\hat{\beta}}(\mathbf{R}_n, \mathbf{R}_m) \cdot (\mathbf{R}_n - \mathbf{R}_m) = \int_{\mathbf{R}_m}^{\mathbf{R}_n} \underline{\hat{\beta}} d\mathbf{R}$ [6,23]. The distance L is the projection of $\mathbf{R}_n - \mathbf{R}_m$ in the diffraction direction, g . $\langle \epsilon_{g,L}^2 \rangle$ is the square of the pair-correlation of lattice distortion in the g direction. The more appropriate term for $\langle \epsilon_{g,L}^2 \rangle$ would be, 'mean square strain-correlation distribution', indicating that this is a function, irreplaceable by a shear number.

Size broadening is an optical scattering effect. When the crystallites become small, the diffraction peaks blow up uniformly in reciprocal space [24]. Assuming equiaxed shape and log-normal size

distribution the size profile can be expressed in a close form [25,26]. Line profiles of faulted and twinned crystals consist of several sub-profiles, where their numbers, shifts and breadths depend on the hkl indices of the fundamental Bragg reflection [27-31]. It was shown by numerical [32] and theoretical [30,31] methods that sub-profiles are the sum of a symmetrical and an anti-symmetrical Lorentzian profile function. The anti-symmetrical Lorentz function is the consequence of interference between two overlapping sub-reflections in reciprocal space, where one and the other correspond to the parent and twin crystal, respectively [30,31].

The contrast factor, C in $\langle \varepsilon_{g,L}^2 \rangle$, in eq. (2), is taking into account the directional dependence of the strength of strain. The hkl dependence of C depends on the relative orientation of the Burgers and line vectors of dislocations, \mathbf{b} and \mathbf{l} , the diffraction vector \mathbf{g} and the elastic constants of the material [33-36]. In polycrystalline materials, the hkl dependent contrast factors have to be averaged over the permutations of the hkl indexes [34,35,37,38]. The averaged contrasts are functions of the fourth order invariants of hkl -s [37]. In cubic and hexagonal crystals, they are [8,37]:

$$\bar{C} = \bar{C}_{h00}(1 - qH^2), \quad \bar{C}_{hk,l} = \bar{C}_{hk,0} [1 + q_1x + q_2x^2], \quad (3)$$

where $H^2 = (h^2k^2 + h^2l^2 + k^2l^2)/(h^2 + k^2 + l^2)^2$, \bar{C}_{h00} and $\bar{C}_{hk,0}$ are the average contrast factor of the $h00$ and $hk,0$ reflections in cubic and hexagonal crystals, $x = (2/3)(l/ga)^2$ and, l and a are the lattice constants of a hexagonal crystal. The q and q_1, q_2 parameters depend on the elastic constants of the crystal and the type of dislocations [36,37]. In ref. [39] the averaged contrasts were evaluated for all crystal systems.

Based on the principles outlined above, diffraction patterns, $I^{PM}(2\theta)$ are modelled using physically established profile functions:

$$I^{PM}(2\theta) = \sum_{hkl} I_{hkl}^S * I_{hkl}^D * I_{hkl}^{PD} * I_{hkl}^{INST} + I_{BG}. \quad (4)$$

The defect related profile functions are the size, I_{hkl}^S , the strain I_{hkl}^D and the planar defect profiles, I_{hkl}^{PD} . The instrumental pattern I_{hkl}^{INST} is measured and the background, I_{BG} added to the model-calculated pattern. We developed the convolutional multiple whole profile (CMWP) software package to simulate the measured diffraction pattern using the physically modelled diffraction pattern in eq. (4) [25,40].

3. Laboratory X-ray diffraction experiments

A large number of laboratory X-ray diffraction experiments used line profile analysis (LPA) to characterize the sub-structure of bulk UFG materials [7,38-64]. Fig. 3a shows the thermal stability of the dislocation density and long-range internal stresses in Ni deformed by HPT to $\varepsilon=58$ applying 8 GPa pressure and 4 rotations [47].

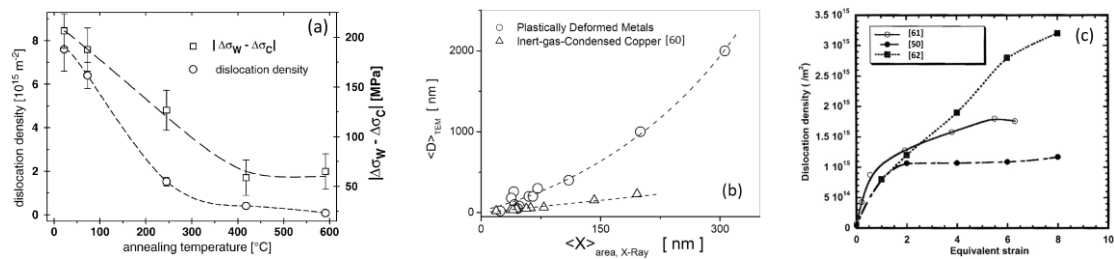


Figure 3. (a) Thermal stability of the dislocation density and long-range internal stresses [47]. (b) Comparison of X-ray crystallite size with TEM grain size [50]. Comparison of X-ray and TEM dislocation densities [52]. (By courtesy of [47,50,52]).

The long-range internal stresses were determined from the peak asymmetries. The grain size was determined by SEM. Both, the dislocation density and the grain size started recovering at about 300 °C. Fig. 3b shows the X-ray and TEM grain size in different UFG materials deformed either by HPT or ECAP along with the grain size in inert-gas condensed Cu measured in the as-received state and after long term natural aging at RT [50]. The figure indicates that in the smallest grain-size region the X-ray and TEM data are identical, whereas when the TEM grain size exceeds about 100 nm the X-ray grain size values tend to show smaller values. TEM grain size gives the true grain-size values, while above about 100 nm X-rays tend to give the sub-grain size. Fig. 3c shows the comparison of dislocation densities in cold rolled Cu determined by TEM [62] or X-ray LPA [61] and ECAP deformed Cu determined by TEM [52]. The figure indicates a good correlation between the data despite the differences in methods, samples and investigators.

4. Synchrotron X-ray diffraction experiments

A relatively large number of synchrotron X-ray diffraction experiments used LPA to characterize the dislocation structure and grain size in bulk UFG materials [65-74]. Lee et al. [70] measured the dislocation density evolution in HPT processed Cu by using synchrotron X-ray diffraction. Fig. 4a shows a typical synchrotron X-ray diffraction pattern. Fig. 4b shows the dislocation density as a function of strain. Authors developed a dislocation-density based constitutive model embedded in a finite element code (FEC). Fig. 4c shows the model calculated and the measured dislocation densities along with data from the literature. The average FEC calculated values (solid red line in Fig. 4c) are in good agreement with the synchrotron XRD values in Fig. 4b and the results in ref. [64] (open squares). The open triangles are TEM calculated dislocation density values taken from ref. [52]. Fig. 4b shows that the dislocation density drops at the largest deformation. The drop at very large HPT deformation values relates most likely to the increased excess vacancy production during HPT processing [76]. Releasing the specimen from the HPT machine, the excess vacancies become free and annihilate some of the stored dislocations, as shown in ref. [76].

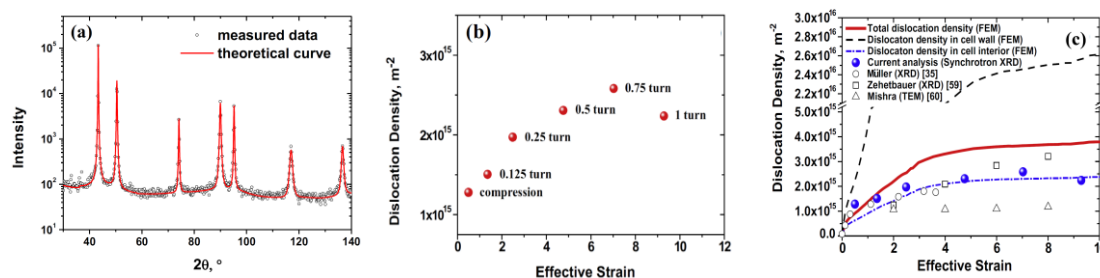


Figure 4. (a) Synchrotron X-ray measured (open circles) and CMWP [40] calculated (solid red line) of an ECAP deformed Cu specimen [72]. (b) Dislocation density values obtained by using the CMWP procedure [40,72]. (c) Finite-element calculated dislocation densities in the cell walls (dashed line), in the cell interiors (dash dot lines) and the total density (solid red line). The full symbols are the same values as in (b). The open symbols are taken from the literature. (By courtesy of Lee et al. [72])

5. Neutron diffraction experiments

The angular resolution of neutron diffractometers is usually substantially lower than that of X-ray diffractometers. During the last two decades spallation neutron sources with considerably improved angular resolution have become perspective equipment for LPA [77-84]. A fully transformed lath-martensite specimen was tensile deformed in-situ in the high resolution and high intensity neutron diffractometer at the TAKUMI beamline of the spallation neutron source J-PARC [84]. In the as-quenched state, the initial crystallite size determined by LPA was 60 nm in good correlation with lath thickness, obtained by TEM. The initial dislocation density was $4.5 \times 10^{15} \text{ m}^{-2}$. The diffraction peaks in the as-quenched state are perfectly symmetrical, see in Fig. 5a. During tensile deformation, the

diffraction peaks become characteristically asymmetric. Peaks with diffraction vectors parallel (see Fig. 5b) or perpendicular to the tensile axis have a longer tail in the smaller or larger d^* direction, where d^* is the reciprocal space coordinate. Similarly, as in the case of tensile deformed Cu single crystals with dislocation cell structures, see refs. [85,86]. Characteristically asymmetric peak broadening indicates the presence of long-range internal stresses between coherent domains within grains. Either these are the lath packets oriented with lath-planes parallel or oblique to the largest Schmid factor directions. In the lath packets oriented parallel to the largest Schmid factor, dislocations glide easily with long mean-free paths. In lath packets oriented oblique to the largest Schmid factor, dislocations are stuck in the lath boundaries and will have short mean-free paths. In the former case, the initial dislocation density is larger than what can carry the strain, therefore it decreases and these packets soften (see the open triangles in Fig. 5c and ref. [57]). In the latter case, even the large initial dislocation density is not sufficient to carry the strain, therefore it increases and these packets harden (see the open circles in Fig. 5c). As a result, plastic deformation divides the lath packets, initially statistically identical, into hard and soft packets and the material behaves like a composite [84].

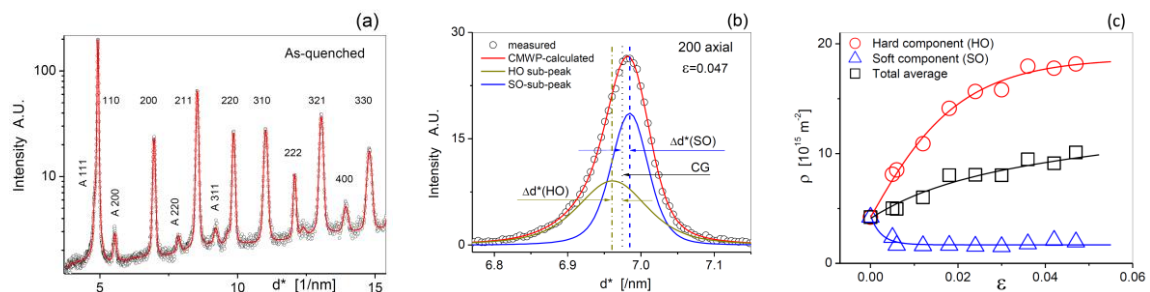


Figure 5. (a) Measured (open circles) and CMWP [40] calculated neutron diffraction pattern of the as-quenched lath martensite. (b) Asymmetric 200 peak when the diffraction vector and the tensile axis are parallel. The figure also shows the long-range internal stresses between soft and hard packets. (c) Evolution of the dislocation densities in the soft (open triangles) and hard (open circles) packets and the average values (open squares) (Figures (b) and (c) by courtesy of [84]).

6. Conclusions

- (1) Line profile analysis developed during the last few decades, being able to provide reliable and physically well-established quantities to characterize the microstructure of plastically deformed materials. This is especially true for UFG materials in which the grain size is small and the defect density large.
- (2) Line profile analysis provides an excellent opportunity for synergetic characterization of microstructures by the simultaneous application of electron microscopy and diffraction. Whether the application of laboratory X-ray, synchrotron X-ray or neutron diffraction, the synergy works.
- (3) Diffraction experiments provide of all kinds internal stresses not easily accessible by electron microscopy methods.

References

- [1] Stokes A R, Wilson A J C 1942 *Proc Camb Phil Soc* **38** 313
- [2] Warren B E 1959 *Progr Metal Phys* **8** 147
- [3] Warren B E 1969 *X-ray Diffraction* New York; Dover.
- [4] Rebuffi L, Troian A, Ciancio R, Carlino E, Amimi A, Leonardi A, Scardi P 2016 *Sci Report* **6** 20712
- [5] Krivoglaz M A 1996 in *Theory of X-ray and Thermal Neutron Scattering by Real Crystals* Plenum Press, New York
- [6] Wilkens M 1970 in *Fundamental Aspects of Dislocation Theory* J.A. Simmons, R. de Wit, R. Bullough (Eds.), vol II, Nat Bur Stand (US) Spec Publ No 317, Washington, DC, USA, p. 1195.

- [7] Ungár T, Borbély A 1996 *Appl Phys Lett* **69** 3173
- [8] Ungár T, Dragomir I, Révész Á, Borbély A 1999 *J Appl Cryst* **32** 992
- [9] Estevez-Rams E, Leoni M, Scardi P, Aragon-Fernandez B, Fuess H 2003 *Philos Mag* **83** (2003) 4045
- [10] Velterop L, Delhez R, de Keijser Th H, Mittemeijer E J, Reefman D J 2000 *Appl Cryst* **33** 296
- [11] Balogh L, Ribárik G, Ungár T *J Appl Phys* **100** 023512
- [12] Balogh L, Tichy G, Ungár T 2009 *J Appl Cryst* **42** 580
- [13] Leineweber A, Mittemeijer E 2006 *Z Kristallographie* **S23** 117
- [14] Leineweber A 2016 *J Appl Cryst* **49** 1632
- [15] Akhlaghi M, Steiner T, Meka S R, Leineweber A, Mittemeijer E J 2015 *Acta Mater* **98** 254
- [16] Langford J I, Boulton A, Auffrédic J P, Louër D 1993 *J Appl Cryst* **26** 22
- [17] Scardi P, Leoni M *Acta Cryst* **A57** 604
- [18] Ungár T 2008 *J Powder Diffr* **23** 125
- [19] Williamson G K, Hall W H 1953 *Acta metall* **1** 22
- [20] Bailey J E, Hirsch P B 1960 *Phil Mag* **5** 485
- [21] Ungár T, Mughrabi H, Wilkens M 1982 *Acta Metall* **30** 1861
- [22] Balogh L, Ungár T, Zhao Y, Zhu Y T, Horita Z, Xu C, Langdon T G 2008 *Acta Mater* **56** 809
- [23] Zilahi Gy, Ungár T, Tichy G 2015 *J Appl Cryst* **48** 418
- [24] James, R W 1965 in *The optical principles of the diffraction of X-ray* Bell G & Sons, Ltd, London
- [25] Ungár T, Gubicza J, Ribárik G, Borbély A 2001 *J Appl Cryst* **34** 298
- [26] Scardi P, Leoni M 2002 *Acta Cryst* **A58** 190
- [27] Balogh L, Ribárik G, Ungár T 2006 *J Appl Phys* **100** 023512-10.
- [28] Balogh L, Tichy G, Ungár T 2009 *J. Appl. Cryst* **42** 580
- [29] Velterop L, Delhez R, de Keijser Th H, Mittemeijera E J, Reefman D 2000 *J Appl Cryst* **33** 296
- [30] Estevez-Rams R, Penton-Madrigal A, Lora-Serrano R, Martinez-Garcia J 2001 *J Appl Cryst* **34** 730
- [31] Estevez-Rams R, Leoni M, Scardi P, Aragon-Fernandez B, Fuess F 2003 *Philosophical Magazine* **83** 4045
- [32] Treacy M M J, Newsam J M, Deem M W 1991 *Proc Roy Soc London* **A433** 499
- [33] Wilkens M 1970 *Phys Stat Sol* **A2** 359
- [34] Klimanek P J, Kuzel R L Jr 1988 *J Appl Cryst* **21** 59
- [35] Kuzel R L Jr, Klimanek P J 1989 *J Appl Cryst* **22** 299
- [36] Borbély A, Dragomir I C, Ribárik G, Ungár T, *J Appl Cryst* **36** 160
- [37] Ungár T, Tichy G 1999 *Phys Stat Sol* **A147** 425
- [38] Révész Á, Ungár T, Borbély A, Lendvai J 1996 *Nanostr Mater* **7** 779
- [39] Leoni M, Martinez-Garcia J, Scardi P 2007 *J Appl Cryst* **40** 719
- [40] Ribárik G, Ungár T 2010 *Mater Sci Eng* **A528** 112
- [41] Islamgaliev R K, Chmelik F, Kuzel R 1997 *Mater Sci Eng* **A234-236** 335
- [42] Islamgaliev R K, Chmelik F, Kuzel R 1997 *Mater Sci Eng* **A27** 43
- [43] Fátay D, E. Bastarash, Nyilas K, Dobatkin S, Gubicza J, Ungár T 2003 *Z Kristallgr* **94** 1
- [44] Zhu Y T, Huang J Y, Gubicza J, Ungár T, Wang Y M, Ma E, Valiev R Z 2003 *J Mater Res* **18** 1908
- [45] Vives S, Gaffet E, Meunier C 2004 *Mater Sci Eng* **A366** 229
- [46] Gubicza J, Nam N H, Balogh L, Hellmig R J, Stoliarov V V, Estrin Y, Ungár T 2004 *Mater Sci Eng* **A378** 248
- [47] Schafler E, Pippin R 2004 *Mater Sci Eng* **A387-389** 799
- [48] Gubicza J, Balogh L, Hellmig R J, Estrin Y, c 2005 *Mater Sci Eng* **A400-401** 334
- [49] Schafler E, Steiner G, Korznikova E, Kerber M, Zehetbauer M J 2005 *Mater Sci Eng* **A410-411** 169
- [50] Ungár T, Tichy G, Gubicza J, Hellmig R J 2005 *Powder Diffr* **55** 366
- [51] Gubicza J, Chinh N G, Langdon T G, Ungár T 2006 *Proc Ultraf Grain Mater IV* Ed Zhu Y T et

al pp 231

- [52] Mishra A, Kad B K, Gregori F, Meyers M A 2007 *Acta Mater* **55** 13
- [53] Ungár T, Schafner E, Hanák P, Bernstorff S, Zehetbauer M J 2007 *Mater Sci Eng* **A462** 398
- [54] Sarkar A, Bhowmik A, Suwas S 2009 *Appl Phys* **A94** 943
- [55] Liu M, Roven H J, Liu X, Murashkin M, Valiev R Z, Ungár T, Balogh L 2010 *J Mater Sci* **45** 4659
- [56] Kerber M B, Zehetbauer M J, Schafner E, Spieckermann F C, Bernstorff S, Ungár T 2011 *JOM* **63** 61
- [57] Ungár T, Li L, Tichy G, Pantleon W, Choo H, Liaw P K 2011 *Scripta Mater* **64** 876
- [58] Yoon E Y, Lee, D J, Kim T S, Chae H J, Jenei P, Gubicza J, Ungár T, Janecek M, Vratna J, Lee S, Kim H S 2012 *J Mater Sci* **47** 7117
- [59] Jóni B, Schafner E, Zehetbauer M J, Tichy G, Ungár T 2013 *Acta Mater* **61** 632
- [60] Skrotzki W, Eschke A, Jóni B, Ungár T, Toth L S, Ivanisenko Yu, Kurmanaeva L 2013 *Acta Mater* **61** 7271
- [61] Bahl S, Suwas S, Ungár T, Chatterjee K 2017 *Acta Mater* **122** 138
- [62] Ungár T, Ott S, Sanders P G, Borbély A, Weertman J R 1998 *Acta Mater* **46** 3693
- [63] Ungár T, Zehetbauer M 1996 *Scripta Mater* **35** 1467
- [64] Zehetbauer M, Seumer V 1993 *Acta Mater* **41** 577
- [65] Zehetbauer M J, Steiner G, Schafner E, Korznikov A, Korznikova E 2006 *Mater Sci Forum* **503-504** 57
- [66] Schafner E, Nyilas K, Bernstorff S, Zeipper L, Zehetbauer M J, Ungár T 2006 *Z Kristallogr Suppl* **23** 129
- [67] Fan G J, Fu L F, Wang Y D, Ren Y, Choo H, Liaw P K, Wang G Y, Browning N D 2006 *Appl Phys Lett* **89** 101918-3
- [68] Li L, Ungár T, Wang Y D, Fan G J, Yang Y L, Jia N, Ren Y, Tichy G, Lendvai J, Choo H, Liaw P K 2009 *Scripta Mater* **60** 317
- [69] Li L, Ungár T, Wang Y D, Morris J R, Tichy G, Lendvai J, Yang Y L, Ren Y, Choo H, Liaw P K 2009 *Acta Mater* **57** 4988
- [70] Barabash R I, Ice G E, Liu W, Barabash O M 2009 *Micron* **40** 28
- [71] Kilmametov A R, Vaughan G, Yavari A R, LeMoulec A, Botta W J, Valiev R Z 2009 *Mater Sci Eng* **A503** 10
- [72] Lee D J, Yoon E Y, Ahn D-H, Park B H, Park H W, Park L J, Estrin Y, Kim H S 2014 *Acta Mater* **76** 281
- [73] Zhang H, Fong K S, Song X, Ying S, Salvati E, Sui T, Korsunsky A M 2016 *Proc Int MConf Eng Comp* ISBN 978-988-14047-6-3
- [74] Miyajima Y, Okubo S, Miyazawa T, Adachi H, Fujii T 2016 *Phil Mag* **96** 294
- [75] Li L, Ungár T, Toth L S, Skrotzki W, Wang J D, Ren J, Choo H, Fogarassy Z, Zhou X Z and Liaw P K 2016 *Metall Mat Trans A* **47** 6632
- [76] Dubravina I, Zehetbauer M, Schafner E, Alexandrov I 2004 *Mater Sci Eng* **A387-389** 817
- [77] Woo W, Choo H, Brown D W, Bourke M A M, Feng Z, David S A, Hubbard C R, Liaw P K 2005 *Appl Phys Lett* **86** 231902-3
- [78] Tao K, Choo H, Li H, Jin J E, Lee Y K 2007 *Appl Phys Lett* **90** 101911-3
- [79] Lukas P, Strunz P, Davydov V, Kuzel R 2009 *ICDD ISSN* **1097-0002** 421
- [80] Woo W, Ungar T, Feng Z, Kenik E, Clausen B 2010 *Metall Mater Transact* **A41** 1210
- [81] González Crespo P A, Luis Pérez C, Hughes D, Turillas X 2013 *J Nanomater* **2013** 404903-6
- [82] Ahmmed K F, Balogh L, Idrees Y, Yu H, Long F, Daymond M R 2016 *J Appl Cryst* **49** 1609
- [83] Harjo S, Kawasaki T, Gong W, Aizawa K 2016 *J Phys Conf Ser* **746** 012046-7
- [84] Ungár T, Harjo S, Kawasaki T, Tomota Y, Ribárik G, Shi Z 2017 *Metall Mater Transact* **A48** 159
- [85] Ungár T, Mughrabi H, Ronnpagel D, Wilkens M 1984 *Acta Metall* **32** 333
- [86] Mughrabi H, Ungár T, Kienle W, Wilkens M 1986 *Phil Mag* **53** 793